First-in-Humans Brain PET Imaging of the GluN2B-Containing N-methyl-D-aspartate Receptor with (R)-^{11}C-Me-NB1

Lucas Rischka*[1], Chrysoula Vraka*[2], Verena Pichler[2,3], Sazan Rasul[2], Lukas Nics[2], Gregor Gryglewski[1], Patricia Handschuh[1], Matej Murgaš[1], Godber M. Godbersen[1], Leo R. Silberbauer[1], Jakob Unterholzner[1], Christoph Wotawa[1], Ahmed Haider[4], Hazem Ahmed[4], Roger Schibli[4], Thomas Mindt[2,5,6], Markus Mitterhauser[2,5], Wolfgang Wadsak[2,7], Andreas Hahn[1], Rupert Lanzenberger[1], Marcus Hacker[2], and Simon M. Ametamey[4]

[1]Department of Psychiatry and Psychotherapy, Medical University of Vienna, Vienna, Austria; [2]Division of Nuclear Medicine, Department of Biomedical Imaging and Image-guided Therapy, Medical University of Vienna, Vienna, Austria; [3]Department of Pharmaceutical Chemistry, University of Vienna, Vienna, Austria; [4]Centre for Radiopharmaceutical Sciences ETH-PSI-USZ, Institute of Pharmaceutical Sciences ETH, Zurich, Switzerland; [5]Ludwig Boltzmann Institute Applied Diagnostics, Vienna, Austria; [6]Institute of Inorganic Chemistry, University of Vienna, Vienna, Austria; and [7]Center for Biomarker Research in Medicine (CBmed), Graz, Austria

The N-methyl-D-aspartate receptor (NMDAR) plays a crucial role in neurodegenerative diseases such as Alzheimer disease and in the treatment of major depression by fast-acting antidepressants such as ketamine. Given their broad implications, GluN2B-containing NMDARs have been of interest as diagnostic and therapeutic targets. Recently, (R)-^{11}C-Me-NB1 was investigated preclinically and shown to be a promising radioligand for imaging GluN2B subunits. Here, we report on the performance characteristics of this radioligand in a first-in-humans PET study. **Methods:** Six healthy male subjects were scanned twice on a fully integrated PET/MR scanner with (R)-^{11}C-Me-NB1 for 120 min. Brain uptake and tracer distribution over time were investigated by SUVs. Test–retest reliability was assessed with the absolute percentage difference and the coefficient of variation. Exploratory total volumes of distribution (V_T) were computed using an arterial input function and the Logan plot as well as a constrained 2-tissue-compartment model with the ratio of rate constants between plasma and tissue compartments (K_1/k_2) coupled (2TCM). SUV was correlated with V_T to investigate its potential as a surrogate marker of GluN2B expression. **Results:** High and heterogeneous radioligand uptake was observed across the entire gray matter with reversible kinetics within the scan time. SUV absolute percentage difference ranged from 6.9% to 8.5% and coefficient of variation from 4.9% to 6.0%, indicating a high test–retest reliability. A moderate correlation was found between SUV averaged from 70 to 90 min and V_T using Logan plot (Spearman $\rho = 0.44$). Correlation between V_T Logan and 2TCM was $r = 0.76$. **Conclusion:** The radioligand (R)-^{11}C-Me-NB1 was highly effective in mapping GluN2B-enriched NMDARs in the human brain. With a heterogeneous uptake and a high test–retest reliability, this radioligand offers promise to deepen our understanding of the GluN2B-containing NMDAR in the pathophysiology and treatment of neuropsychiatric disease such as Alzheimer disease and major depression. Additionally, it could help in the selection of appropriate doses of GluN2B-targeting drugs.

Key Words: glutamate; N-methyl-d-aspartate (NMDA); GluN2B subunits; neurodegenerative disease; PET

The N-methyl-D-aspartate receptor (NMDAR) constitutes a heterotetrameric glutamate-gated ion channel that mediates key physiologic functions such as synaptic transmission, plasticity, and higher cognitive functions in the mammalian central nervous system (1,2). Despite their homeostatic relevance, NMDARs trigger pathophysiologic processes on excessive activation, thereby prompting apoptotic cascades that ultimately result in neurodegeneration (3). Moreover, NMDAR dysfunctions have been implicated in a multitude of neuropsychiatric disorders including Alzheimer disease, vascular dementia, Parkinson disease, stroke, traumatic brain injury, depression, and schizophrenia (4,5). Recent studies demonstrated that activation of extrasynaptic NMDARs, which are typically enriched with the GluN2B subunit, resulted in excitotoxicity, whereas activation of synaptic NMDARs had protective effects (4). As such, subtype-selective modulation of GluN2B-containing NMDARs has been suggested as a promising drug development strategy that would provide therapeutic efficacy, while concurrently sparing physiologic NMDAR functions (6,7). Despite strenuous research and development efforts, GluN2B-selective antagonists showed only limited clinical efficacy so far (8). Although underlying causes may have been of multifactorial origin, it has been suggested that the availability of an appropriate GluN2B-targeted probe would facilitate drug development (9). Indeed, a radioligand to visualize GluN2B-containing NMDARs in the living human brain is currently lacking. Thus, it is of paramount value to develop such tools to further elucidate the versatile roles of GluN2B-containing NMDARs in neurodegenerative and other neuropsychiatric diseases, as well as to guide future drug development efforts via target engagement studies.

Despite the plethora of attempts to develop a suitable NMDAR PET radioligand, most reported probes suffered from major drawbacks such as low brain uptake, radiometabolites entering the brain, prominent off-target binding particularly to σ1 receptors, and brain uptake inconsistent with the known expression profile (10,11). To date, the most promising structural class of GluN2B-targeted PET radioligands are the 2,3,4,5-tetrahydro-1H-benzazepine derivatives (12–15). A recent publication by Haider et al. reported on the

benzazepine derivative (R)-^{11}C-Me-NB1 (Fig. 1) as a potential PET radioligand for imaging the GluN2B-containing NMDARs. Biodistribution and PET imaging studies in rodents showed an uptake pattern in brain regions known to express the GluN2B subunits of the NMDAR, with the lowest uptake in the cerebellum, a brain region known to have low to negligible GluN2B subunits in rodents. Specificity of (R)-^{11}C-Me-NB1 binding was substantiated in blocking studies in a dose-dependent manner, and selectivity over σ1 receptors was confirmed using σ1 receptor knockout mice (15).

Considering the promising characteristics of this radioligand in rodents, the current work aims to translate the utility of (R)-^{11}C-Me-NB1 for imaging the GluN2B subunits of the NMDAR to humans. To the best of our knowledge, this work signifies the first assessment of a GluN2B PET imaging probe in the living human brain.

MATERIALS AND METHODS

Participants and Study Design

Six healthy male subjects (mean age ± SD, 23.3 ± 2.9) were recruited for the study. All participants were free from internal, neurologic, or psychiatric disorders assessed via a thorough medical history, physical examination, electrocardiogram, and routine laboratory parameters. Exclusion criteria were neurologic diseases or psychiatric disorders; illness 2 wk before recruitment; history of drug or atopic allergy; myocardial infarction; history of cancer or liver or renal disease; family history of prolonged QT interval; MRI or PET contraindications; consumption of tobacco products 3 mo before recruitment; history of drug or alcohol abuse; and significant prior radiation exposure in the past 10 y. After detailed explanation of the study design, all subjects gave written informed consent. The study was registered in the EudraCT database (2018-002933-39) and approved by the Ethics Committee of the Medical University of Vienna (ethics no. 1980/2018). Procedures were performed in accordance with the Declaration of Helsinki. Subjects were reimbursed for participation.

Tracer Preparation

(R)-^{11}C-Me-NB1 was produced on a fully automated Tracerlab FX2 C synthesis module (GE Healthcare) by applying ^{11}C-CO$_2$ from a PETtrace 860 (GE Healthcare). ^{11}C-CH$_3$I was reacted with the enantiomerically pure des-methyl good manufacturing practice–grade precursor (R)-NB1 in dimethylformamide and in the presence of Cs$_2$CO$_3$ following previously published procedures (15). Minor synthetic adaptations included the use of a SupelcosilTM LC-ABZ+ column (5 μm, 250 × 10 mm; Bellonte) and a mobile phase of 60% acetonitrile/40% aqueous Na$_2$HPO$_4$ (0.02 mol/L) for the final product purification. After high-performance liquid chromatography (HPLC) purification, the product was trapped on a Sep-Pak Plus, C18 Cartridge (Waters), washed with 10 mL of H$_2$O for injection, eluted with 1.5 mL of ethanol, and formulated for human application using 10 mL of NaCl (0.9%) and 6 mL of phosphate-buffered saline. Product quality was assessed according to the guidance of radiopharmaceutical preparations of the European Pharmacopoeia (16). Molar activities were calculated through assessment of radioactivity at the

FIGURE 1. Chemical structure of (R)-^{11}C-Me-NB1.

end of synthesis and determination of nonradioactive (R)-Me-NB1 via HPLC. Values were decay-corrected to the time of tracer administration.

PET Imaging

All participants underwent 2 measurements on a fully integrated PET/MR scanner (mMR Biograph; Siemens) lasting for 120 min. The mean interval between the scans was 18.2 ± 8.8 d (range, 6–28 d), and measurements started between 4:30 and 6:00 PM (central European time; mean difference between the measurement start times, 21 ± 24 min; range, 0–60 min). PET data were acquired in 3-dimensional list-mode. The radioligand (R)-^{11}C-Me-NB1 was administered as a bolus through a cubital vein (mean injected dose, 448 ± 34 MBq; 5.98 ± 0.85 MBq/kg of body weight; 0.15 ± 0.11 nmol/kg of body weight; 1 value was excluded because of technical HPLC issues). There were no adverse events or clinically detectable pharmacologic effects in any of the subjects. No changes in vital signs, laboratory results, or electrocardiograms were observed. During the scan, subjects were instructed not to fall asleep, to observe a black crosshair on a gray background presented on a screen at the end of the gantry, to let their thoughts wander, and to not move any body part. Additionally, head movement was minimized with stabilizing cushions within the head coil.

Arterial Blood Sampling, Metabolite Analyses, and Arterial Input Function

Before each measurement, arterial and venous cannulas were inserted in the radial artery and a cubital vein of the opposite arm for arterial blood sampling and administration of the radioligand. Arterial blood was drawn automatically for the first 6 min (Twilite II system; Swisstrace). Manual blood samples were taken at 3, 4, 5, 10, 20, 30, 40, 60, 80, 100, and 120 min and were immediately measured in a γ-counter (Wizard^2, 3$''$; Perkin Elmer), for whole blood activity and, after centrifugation, for plasma activity. The γ-counter was cross-calibrated to the PET/MR scanner. Radiometabolites were determined for the time points 5, 10, 20, 30, 40, and 60 min by HPLC using an Agilent 1260 Infinity system (pumps, degasser and ultraviolet detector) connected to a motorized valve (BESTA; Motorventil) and a radiodetector (RamonaStar; Elysia-Raytest). A column switching method (17) was used to concentrate a lipophilic radiometabolite and the parent compound, while a more hydrophilic radiometabolite eluted from the column. Up to 5 mL of plasma were directly injected into the HLB OASIS column (OASIS resin; Waters) with the mobile phase consisting of 1% acetonitrile and water. In an initial pilot study, a recovery rate of 99.6% was observed for the parent compound. After pump switching, the HLB OASIS column was back-flushed with a mobile phase consisting of 60% acetonitrile and 40% 50 mM ammonium acetate, pH 9. The second radiometabolite was separated from the parent compound using a XSelect column (HSS T3, 3.5 μm, 100 × 4.6 mm; Waters) equipped with the corresponding precolumn. The areas under the curves were decay-corrected. The parent compound was identified by the retention time of the reference standard.

MRI

Simultaneously with the PET acquisition, a structural T1-weighted image was acquired with a magnetization prepared rapid gradient echo sequence (echo time/repetition time = 4.21/2,200 ms, inversion time = 900 ms, flip angle = 9°, 160 sagittal slices, voxel size = 1 × 1 × 1.1 mm) for attenuation correction of the PET data and spatial normalization and to rule out structural abnormalities.

PET Processing

PET data were reconstructed with an ordinary Poisson ordered-subset expectation maximization algorithm (3 iterations, 21 subsets) and binned into 12 × 5, 6 × 10, 3 × 20, 6 × 30, 9 × 60, 15 × 300, and 3 × 600 s frames. In addition to standard corrections, data were

corrected for attenuation and scatter with a pseudo-CT approach (*18*) based on the structural MRI of the first measurement.

Preprocessing was performed with SPM12 (Wellcome Trust Centre for Neuroimaging), as previously described (*19*). Briefly, PET data were corrected for head motion (quality setting = 1) and coregistered to the structural MRI. The structural MRI was spatially normalized to MNI space, and the transformation matrix was applied to the coregistered PET images.

Regions of Interest (ROIs)

Time–activity curves were extracted for the following ROIs from the Harvard-Oxford atlas and the probabilistic cerebellar atlas (https://fsl.fmrib.ox.ac.uk/fsl/fslwiki/Atlases): frontal, temporal, parietal, occipital, cingulate, and somatosensory cortex as well as the subcortical regions thalamus, striatum, amygdala, and hippocampus and the cerebellar gray matter, excluding the vermis. Additionally, the white matter structures centrum semiovale (extracted from the SPM12 tissue probability map), corpus callosum (from the Hammers N30R83 atlas (*20*)), and the cerebellar white matter (*21*) were investigated (Fig. 2, top row). The left and corresponding right side of each ROI were averaged.
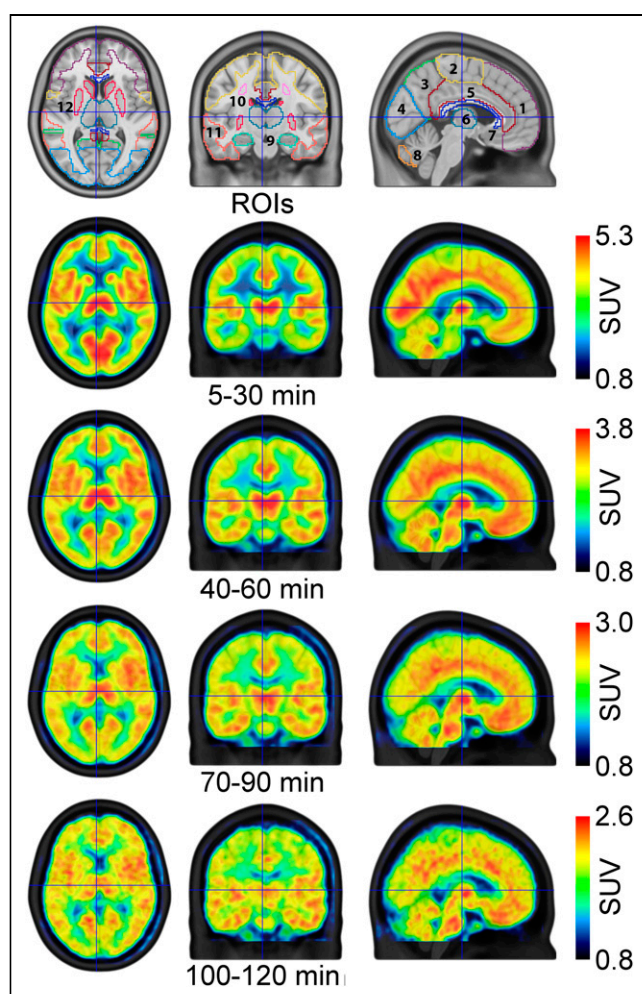

FIGURE 2. ROIs and SUV$_{mean}$ maps. First row depicts investigated ROIs covering cortical, subcortical, and white matter structures: 1, frontal cortex; 2, somatosensory cortex; 3, parietal cortex; 4, occipital cortex; 5, cingulate cortex; 6, thalamus; 7, corpus callosum; 8, cerebellar gray matter; 9, hippocampus; 10, centrum semiovale; 11, temporal cortex; 12, striatum. Amygdala and cerebellar white matter are not visible in the presented slices (MNI space, x = −4, y = 16, z = 7 mm). Remaining rows depict radioligand distribution in terms of SUV for various time points (averaged across subjects).

Brain Uptake

To investigate brain uptake and tracer distribution over time, SUVs were computed as activity concentration in tissue divided by administered dose per kilogram of body weight. For further analyses and demonstration purposes, SUV time–activity curves and SUV voxelwise maps were averaged for the time points 5–30, 40–60, 70–90, and 100–120 min.

In an exploratory approach, NMDAR binding (total volume of distribution, V_T) was quantified with the Logan plot using PMOD 4.2 (PMOD Technologies Ltd.; www.pmod.com). For potential clinical applicability with high patient comfort, only the first 90 min of the data were used for the estimation of V_T. The start time of the fit of the Logan plot (t*) could not be determined automatically for the centrum semiovale because of high noise levels. Hence, the t* of the corpus callosum was used due to similar kinetics (Fig. 3). A time–stability analysis was performed from 40 to 120 min for 4 regions with varying uptake (temporal and parietal cortex, striatum, and hippocampus) to verify that measuring for 90 min is suitable.

A second exploratory analysis was conducted, quantifying V_T with a constrained 2-tissue-compartment model with the ratio of rate constants between plasma and tissue compartments (K_1/k_2) coupled (2TCM) for a measurement duration of 90 min. K_1/k_2 was estimated across all gray matter regions because of different kinetics in the white matter regions.

Statistics

To assess the test–retest reliability, absolute percentage difference (APD), as well as the coefficient of variation (COV), were calculated between the 2 measurements for each ROI. Since there is no ground truth, the APD was determined as APD[%] = |m1 − m2|/((m1 + m2)/2) × 100. COV[%] was calculated as (SD/mean) × 100. The intraclass correlation coefficient for absolute agreement was computed for each region of the averaged SUV time points. SUV averaged from 70 to 90 min was correlated with V_T Logan plot estimated for 90 min across all ROIs. Finally, V_T Logan plot for 90 min was correlated with V_T 2TCM.

RESULTS

Radiochemistry

After sterile filtration at the end of synthesis, 4.16 ± 1.31 GBq of (*R*)-^{11}C-Me-NB1 was obtained with a radiochemical purity of 97.5% ± 1.6%. Molar activity ranged from 35 to 1,115 GBq/μmol (1 value was excluded because of technical HPLC issues). All preparations were within the limits set by the European Pharmacopoeia.

Blood Data Analysis

(*R*)-^{11}C-Me-NB1 was metabolized with 29.6% ± 5.5% of the parent fraction left after 20 min and 15.7% ± 3.3% after 40 min (Supplemental Fig. 1A; supplemental materials are available at http://jnm.snmjournals.org). Two radioactive metabolites were identified, which were more polar than the parent radioligand and showed baseline separation on the HPLC chromatograms (Supplemental Figs. 1B and 1C).

Brain Uptake

The radioligand exhibited reversible pharmacokinetics (see the rate constant from compartment representing specific binding to compartment representing nondisplaceable binding in tissue [k_4] obtained from 2TCM below) within the measurement time, and an area-specific brain uptake pattern was observed (Figs. 2, 3, and 4). At peak (~15–20 min after injection), SUV was highest in the striatum (4.5) and lowest in the white matter regions centrum semiovale and corpus callosum (both 1.8), followed by cerebellar white matter (2.6). Cortical regions showed similar kinetics, particularly after 60 min. In contrast, the kinetics of centrum semiovale and corpus callosum varied markedly from the other regions (Fig. 3). SUV$_{mean}$ time–activity curves and SD of representative regions are depicted in Supplemental Figure 2.
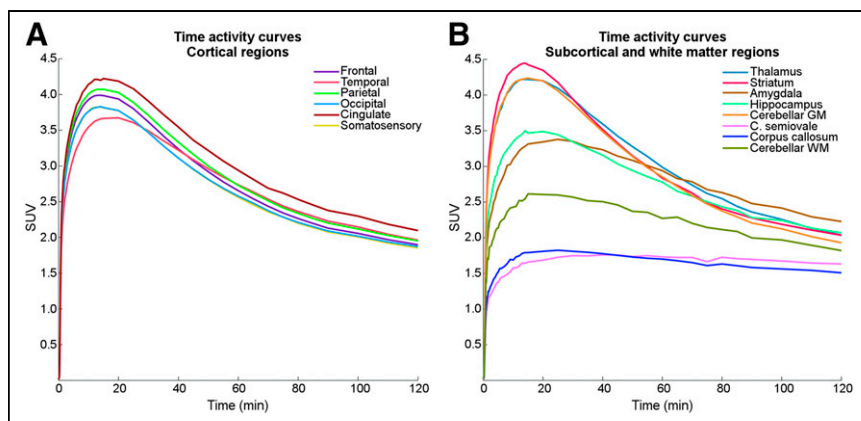
FIGURE 3. Kinetics of (R)-^{11}C-Me-NB1. Reversible kinetics were obtained within measurement time. (A) Time–activity curves demonstrate homogeneous kinetics in cortical regions. (B) Subcortical regions showed variable kinetics, with highest uptake observed in striatum. Lowest SUV and markedly different kinetics were observed in centrum semiovale and corpus callosum.

The time–stability analysis of the exploratory Logan plot revealed that measuring for 90 min is feasible with an underestimation of approximately 10% (Supplemental Fig. 3, solid line). In addition, t* was evaluated as a function of measurement time (dashed line). Logan plots of 1 representative subject are depicted in Supplemental Figure 4 to show linearity. The V_T of the Logan plot varied between 12.8 in the corpus callosum and 19.0 mL/cm^{-3} in the amygdala (Fig. 4B). The average V_T across all regions was comparable between the first and second measurement (15.2 vs. 15.9 mL/cm^{-3}).

For the 2TCM, the model did not converge for white matter regions (i.e., centrum semiovale, corpus callosum, and cerebellar white matter). One subject did not show reasonable V_T in 1 measurement and was therefore excluded from further analyses. The 2TCM confirmed the reversible binding with k_4 between 0.02 (somatosensory cortex) and 0.04 (cerebellar gray matter). V_T 2TCM was slightly higher than with the Logan plot (Supplemental Fig. 5).

A moderate correlation was achieved between Logan plot 90 min and SUV 70–90 min (Spearman ρ = 0.44). Spearman rank correlation was used because of the presence of an outlier in V_T in the test–retest analysis (Fig. 5C). The correlation between V_T Logan and 2TCM was good (r = 0.76) with the caveat of 1 excluded subject and only gray matter regions (Supplemental Fig. 5).

Test–Retest Reliability

High test–retest reliability was obtained for SUVs with slightly increasing values over time. Average APD across all ROIs was 6.9% versus 8.5% for SUV 5–30 min versus 100–120 min and COV was 4.9% versus 6.0% (Fig. 5A). The intraclass correlation coefficient decreased from excellent (0.85 SUV 5–30 min) to moderate (0.58 SUV 100–120 min)

For V_T Logan plot, the variability was slightly higher (mean APD 10.5%, mean COV 7.4%), which is caused by the same subject that did not show reasonable V_T in the 2TCM (Fig. 5B). In comparison, for V_T 2TCM, mean APD was 8.2% and mean COV 5.8%, slightly lower than with Logan plot (1 subject excluded, only gray matter regions). Investigation of the medians in Figure 5A and 5B exhibits similar APD between SUV and V_T except for the centrum semiovale and the corpus callosum.

Complete lists of the SUVs for the various time points, V_T for Logan plot, and 2TCM for the test and retest measurement, alongside the values for APD and COV, are shown in Supplemental Tables 1–4.

DISCUSSION

In this study, the potential of (R)-^{11}C-Me-NB1, a selective and specific radioligand for imaging the GluN2B subunits of the NMDAR in rodents, was examined for its performance characteristics in humans and utility in a clinical setting.

(R)-^{11}C-Me-NB1 has several advantages over previously published GluN2B PET radioligands (10). These include high specificity to the target receptor and topologic distribution that matches the known expression pattern (22,23). Furthermore, the radioligand is easily and efficiently synthesized in good radiochemical yields using a 1-step synthetic approach.

The results of the metabolite analysis showed the presence of 2 hydrophilic radiolabeled compounds, which were more polar than parent (R)-^{11}C-Me-NB1 and likely unable to cross the blood–brain barrier. This reasoning is based on previous studies in rodents that showed that more than 95% of radioactivity in rodent brain was intact (R)-^{11}C-Me-NB1 (14). In a recent study using mice liver microsomes, glucuronidation of the benzylic hydroxyl group and hydroxylation of the aromatic moiety in Me-NB1 were reported. Although we did not identify the radiometabolites, the HPLC profile suggests that the 2 hydrophilic radiometabolites may correspond to a hydroxylated species and the glucuronide of (R)-^{11}C-Me-NB1, respectively (24).
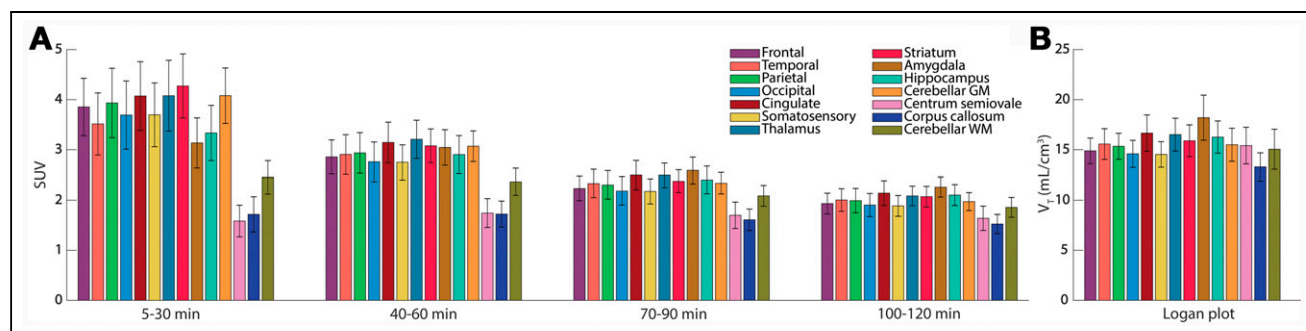

FIGURE 4. SUV and V_T using Logan plot. (A) SUV of each ROI for several time points. (B) Exploratory V_T computed with Logan plot.
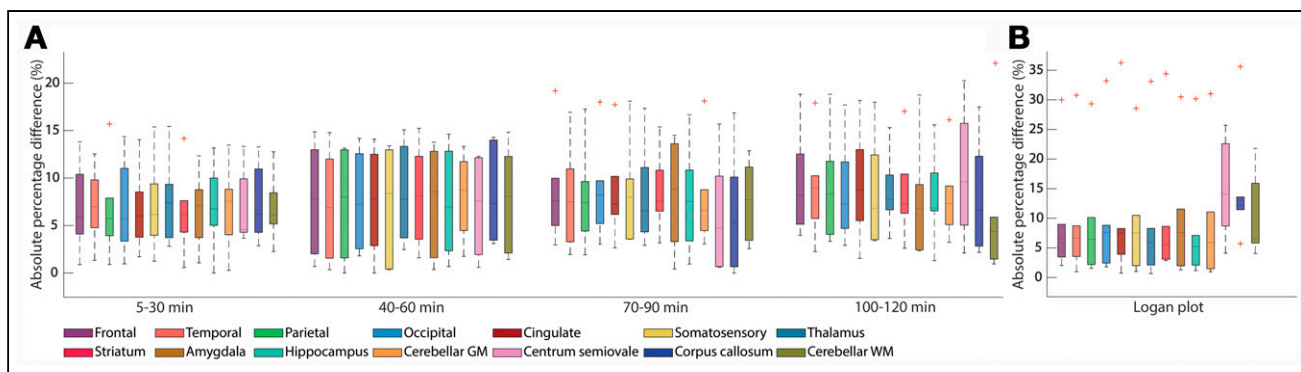
FIGURE 5. Absolute percentage difference (APD) of SUV and Logan plot. (A) APD of SUV is comparable over time in most regions with slightly larger interquartile ranges for 40–60 min. (B) APD of Logan plot visualizes similar median differences as for SUV but with 1 outlier.

Brain uptake and distribution of (R)-^{11}C-Me-NB1 in humans were similar to those in rodent studies in most brain regions, including the cortex, striatum, and thalamus. However, although the cerebellum exhibited generally low radioligand uptake in rodents (*14*), cerebellar uptake in humans was region-dependent. Indeed, whereas the cerebellar white matter was among regions with limited tracer uptake, the cerebellar gray matter exhibited high (R)-^{11}C-Me-NB1 uptake in the present study. Whether the cerebellar uptake of (R)-^{11}C-Me-NB1 in humans reflects specific binding would need to be confirmed in blocking studies with GluN2B antagonists such as CP-101,606.

An important feature of a useful radioligand is the pharmacokinetic profile for absolute quantification. In this regard, (R)-^{11}C-Me-NB1 exhibited reversible binding to the GluN2B-enriched NMDAR, which was quantifiable with the Logan plot and 2TCM. The moderate correlation between V_T and SUV 70–90 min might indicate a substitution of the absolute quantification although this requires further validation, including a comprehensive assessment of different modeling strategies.

Another benefit is the high test–retest reliability of around 8% (APD) for SUV and V_T 2TCM and 11% for V_T Logan plot, for a desirable measurement time of 90 min. The reliability is similar to that of other successfully translated radioligands (*25*), making it a promising tool for clinical applications.

We acknowledge the small sample size of 6 subjects but suggest that this is acceptable for a first proof-of-concept study in humans. A limitation is that only young men were included. Hence, further work is required to assess potential sex differences and alterations with age.

The possibility to map GluN2B-enriched NMDAR in humans now enables receptor occupancy studies for drug development to treat neurodegenerative and other neuropsychiatric diseases. The notion is to modulate GluN2B-containing NMDAR with selective antagonists. However, substances such as EVT-101 or CERC-301 did show in vitro but not in vivo displacement of (R)-^{11}C-Me-NB1 in rodents (*14*) and limited efficacy in humans for CERC-301 (*8*). In contrast, CP-101,606 competed with (R)-^{11}C-Me-NB1 in rodents (*14*) and demonstrated antidepressant effects similar to ketamine in a clinical trial (*26*). However, the further development of the GluN2B antagonist was discontinued because of side effects (*27*). Hence, GluN2B-specific radioligands could aid the clinical investigations of the mechanism of action behind these drugs and the correlation between efficacy and receptor occupancy.

CONCLUSION

For the first time (to our knowledge), a GluN2B subunit NMDAR-specific radioligand showing valuable characteristics in terms of pharmacokinetics and brain uptake was successfully translated into humans. A heterogeneous brain uptake with a robust test–retest variability ($<10\%$) was demonstrated. In an exploratory analysis, we showed that absolute quantification of the total volume of distribution with the Logan plot is feasible. The results suggest that (R)-^{11}C-Me-NB1 is a promising radioligand for visualizing the GluN2B-containing NMDARs in humans and potentially could be used in drug development programs to select appropriate doses of GluN2B-targeting drugs.

KEY POINTS

QUESTION: Is (R)-^{11}C-Me-NB1 a suitable radioligand to map the GluN2B- NMDAR in the human brain?

PERTINENT FINDINGS: The radioligand demonstrated an area-specific brain uptake pattern with reversible pharmacokinetics and a high test–retest reliability.

IMPLICATIONS FOR PATIENT CARE: The possibility to map the GluN2B subunits of NMDAR provides new opportunities for the treatment of neuropsychiatric disorders such as Alzheimer disease and major depression in terms of drug development.

REFERENCES

1. Dingledine R, Borges K, Bowie D, Traynelis SF. The glutamate receptor ion channels. *Pharmacol Rev.* 1999;51:7–61.
2. Bliss TVP, Collingridge GL. A synaptic model of memory: long-term potentiation in the hippocampus. *Nature.* 1993;361:31–39.
3. Sattler R, Tymianski M. Molecular mechanisms of calcium-dependent excitotoxicity. *J Mol Med.* 2000;78:3–13.
4. Hardingham GE, Bading H. Synaptic versus extrasynaptic NMDA receptor signalling: implications for neurodegenerative disorders. *Nat Rev Neurosci.* 2010;11:682–696.
5. Ikonomidou C, Turski L. Why did NMDA receptor antagonists fail clinical trials for stroke and traumatic brain injury? *Lancet Neurol.* 2002;1:383–386.
6. Mony L, Kew JNC, Gunthorpe MJ, Paoletti P. Allosteric modulators of NR2B-containing NMDA receptors: molecular mechanisms and therapeutic potential. *Br J Pharmacol.* 2009;157:1301–1317.
7. Ahmed H, Haider A, Ametamey SM. N-methyl-D-Aspartate (NMDA) receptor modulators: a patent review (2015-present). *Expert Opin Ther Pat.* 2020;30:743–767.
8. Ibrahim L, Diaz Granados N, Jolkovsky L, et al. A randomized, placebo-controlled, crossover pilot trial of the oral selective NR2B antagonist MK-0657 in patients with treatment-resistant major depressive disorder. *J Clin Psychopharmacol.* 2012;32:551–557.
9. Gruber S, Ametamey SM. Imaging the glutamate receptor subtypes: much achieved, and still much to do. *Drug Discov Today Technol.* 2017;25:27–36.
10. Fuchigami T, Nakayama M, Yoshida S. Development of PET and SPECT probes for glutamate receptors. *ScientificWorldJournal.* 2015;2015:716514.
11. Fu H, Tang W, Chen Z, et al. Synthesis and preliminary evaluations of a triazole-cored antagonist as a PET imaging probe ([^{18}F]N2B-0518) for GluN2B subunit in the brain. *ACS Chem Neurosci.* 2019;10:2263–2275.
12. Ahmed H, Haider A, Varisco J, et al. Structure–affinity relationships of 2,3,4,5-Tetrahydro-1 H -3-benzazepine and 6,7,8,9-Tetrahydro-5 H -benzo[7]annulen-7-amine analogues and the discovery of a radiofluorinated 2,3,4,5-Tetrahydro-1 H -3-benzazepine congener for imaging GluN2B subunit-containing N-Methyl-d-Aspartate receptors. *J Med Chem.* 2019;62:9450–9470.
13. Ahmed H, Wallimann R, Haider A, et al. Preclinical development of ^{18}F-OF-NB1 for imaging GluN2B-containing N-Methyl-D-Aspartate receptors and its utility as a biomarker for amyotrophic lateral sclerosis. *J Nucl Med.* 2021;62:259–265.
14. Haider A, Herde AM, Krämer SD, et al. Preclinical evaluation of benzazepine-based PET radioligands (R)- and (S)-^{11}C-Me-NB1 reveals distinct enantiomeric binding patterns and a tightrope walk between GluN2B- and σ1-receptor-targeted PET imaging. *J Nucl Med.* 2019;60:1167–1173.
15. Krämer SD, Betzel T, Mu L, et al. Evaluation of 11 C-Me-NB1 as a potential PET radioligand for measuring GluN2B-containing NMDA receptors, drug occupancy, and receptor cross talk. *J Nucl Med.* 2018;59:698–703.
16. *Radiopharmaceutical Preparations (Radiopharmaceutica, 8.0/1483). European Pharmacopoeia (Europäisches Arzneibuch).* 8th ed. Vienna, Austria: Official Austrian Version, Verlag Oesterreich GmbH; 2008; 1167–1173 (8. Ausgabe Grundwerk).
17. Vasdev N, Collier T. Design and prototype of an automated column-switching HPLC system for radiometabolite analysis. *Pharmaceuticals (Basel).* 2016;9:51.
18. Burgos N, Cardoso MJ, Thielemans K, et al. Attenuation correction synthesis for hybrid PET-MR scanners: application to brain studies. *IEEE Trans Med Imaging.* 2014;33:2332–2341.
19. Rischka L, Gryglewski G, Pfaff S, et al. Reduced task durations in functional PET imaging with [^{18}F]FDG approaching that of functional MRI. *Neuroimage.* 2018;181:323–330.
20. Gousias IS, Rueckert D, Heckemann RA, et al. Automatic segmentation of brain MRIs of 2-year-olds into 83 regions of interest. *Neuroimage.* 2008;40:672–684.
21. van Baarsen KM, Kleinnijenhuis M, Jbabdi S, Sotiropoulos SN, Grotenhuis JA, van Cappellen van Walsum AM. A probabilistic atlas of the cerebellar white matter. *Neuroimage.* 2016;124:724–732.
22. Rigby M, Le Bourdellès B, Heavens RP, et al. The messenger RNAs for the N-methyl-D-aspartate receptor subunits show region-specific expression of different subunit composition in the human brain. *Neuroscience.* 1996;73:429–447.
23. Enoch MA, Rosser AA, Zhou Z, Mash DC, Yuan Q, Goldman D. Expression of glutamatergic genes in healthy humans across 16 brain regions; Altered expression in the hippocampus after chronic exposure to alcohol or cocaine. *Genes Brain Behav.* 2014;13:758–768.
24. Börgel F, Galla F, Lehmkuhl K, Schepmann D, Ametamey SM, Wünsch B. Pharmacokinetic properties of enantiomerically pure GluN2B selective NMDA receptor antagonists with 3-benzazepine scaffold. *J Pharm Biomed Anal.* 2019;172:214–222.
25. Nord M, Finnema SJ, Schain M, Halldin C, Farde L. Test-retest reliability of [^{11}C]AZ10419369 binding to 5-HT(1B) receptors in human brain. *Eur J Nucl Med Mol Imaging.* 2014;41:301–307.
26. Preskorn SH, Baker B, Kolluri S, Menniti FS, Krams M, Landen JW. An innovative design to establish proof of concept of the antidepressant effects of the NR2B subunit selective N-Methyl-D-aspartate antagonist, CP-101,606, in patients with treatment-refractory major depressive disorder. *J Clin Psychopharmacol.* 2008;28:631–637.
27. Machado-Vieira R, Henter ID, Zarate CA. New targets for rapid antidepressant action. *Prog Neurobiol.* 2017;152:21–37.